Reconstructability of Three-Dimensional Upper-Ocean Circulation from SWOT Sea Surface Height Measurements

BO QIU AND SHUIMING CHEN

Department of Oceanography, University of Hawai'i at Mānoa, Honolulu, Hawaii

PATRICE KLEIN

Laboratoire de Physique des Oceans, Ifremer/CNRS/UBO/IRD, Plouzane, France

CLEMENT UBELMANN AND LEE-LUENG FU

Jet Propulsion Laboratory, California Institute of Technology, Pasadena, California

HIDEHARU SASAKI

Application Laboratory, JAMSTEC, Yokohama, Japan

(Manuscript received 30 September 2015, in final form 2 January 2016)

ABSTRACT

Utilizing the framework of effective surface quasigeostrophic (eSQG) theory, this study explores the potential of reconstructing the 3D upper-ocean circulation structures, including the balanced vertical velocity w field, from high-resolution sea surface height (SSH) data of the planned Surface Water and Ocean Topography (SWOT) satellite mission. Specifically, the authors utilize the $^1/_{30}°$, submesoscale-resolving, OFES model output and subject it to the SWOT simulator that generates the along-swath SSH data with expected measurement errors. Focusing on the Kuroshio Extension region in the North Pacific where regional Rossby numbers range from 0.22 to 0.32, this study finds that the eSQG dynamics constitute an effective framework for reconstructing the 3D upper-ocean circulation field. Using the modeled SSH data as input, the eSQG-reconstructed relative vorticity ζ and w fields are found to reach a correlation of 0.7–0.9 and 0.6–0.7, respectively, in the 1000-m upper ocean when compared to the original model output. Degradation due to the SWOT sampling and measurement errors in the input SSH data for the ζ and w reconstructions is found to be moderate, 5%–25% for the 3D ζ field and 15%–35% for the 3D w field. There exists a tendency for this degradation ratio to decrease in regions where the regional eddy variability (or Rossby number) increases.

1. Introduction

Following the launch of the TOPEX/Poseidon (T/P) mission in 1992, nadir-looking satellite altimetry has revolutionized how ocean research is conducted. The maturity of the satellite altimetry technology and the 23-yr accumulation of the high-quality sea surface height (SSH) data from the subsequent missions (i.e., the T/P Extended Mission, *Jason-1*, and OSTM/*Jason-2* missions) have provided us now with an unprecedented opportunity to investigate detailed evolutions of the global and regional ocean circulation and sea level changes from the intraseasonal to decadal time scales. Indeed, through the efforts by both the satellite mission science working teams and the research community at large, a tremendous advancement in our understanding of the ocean circulation and sea level changes with a wide range of temporal and spatial scales has been achieved. For recent review articles on such advancement, see Fu et al. (2010), Morrow and Le Traon (2012), and the references cited therein.

A critical limitation of the nadir-looking altimetry is its 200–300-km spacing between the satellite ground tracks. Even with combined data merged from multiple altimeters, the spatial resolution in a two-dimensional

Corresponding author address: Dr. Bo Qiu, Department of Oceanography, University of Hawai'i at Mānoa, 1000 Pope Road, Honolulu, HI 96822.
E-mail: bo@soest.hawaii.edu

DOI: 10.1175/JPO-D-15-0188.1

SSH map is typically on the order of 200 km in wavelength (Ducet et al. 2000; Chelton et al. 2011). This length scale is inadequate to fully capture the mesoscale oceanic signals that contain 90% of the kinetic energy of the ocean and misses completely the submesoscale oceanic features that have length scales between 10 km and the Rossby radius of deformation of $O(100)$ km. Upper-ocean processes with the length scales of $O(10–200)$ km are dynamically important because they determine the equilibrium state of the upper ocean through the turbulent kinetic energy cascade and energy dissipation (Ferrari and Wunsch 2009). They are also crucial to how the surface ocean communicates with the subsurface interior ocean, affecting the mixed layer (ML) evolution and upper-ocean thermal anomalies (e.g., Lapeyre et al. 2006; Capet et al. 2008; Klein et al. 2008). In addition to the physical properties, upper-ocean meso- and submesoscale processes impact the CO_2 uptake, nutrient supply, and biogeochemistry of the upper ocean as well (e.g., Mahadevan and Archer 2000; Lévy et al. 2001, 2012; Pascual et al. 2015).

To improve the spatial resolution of global SSH measurements, NASA and CNES have recently put forward the Surface Water and Ocean Topography (SWOT) satellite mission that uses Ka-band radar interferometry to produce a 120-km-wide swath of surface elevation measurements. Scheduled for launch in October 2020, SWOT is expected to capture, on a global average, the oceanic meso- and submesoscale circulation features at spectral wavelength scales of $\geq$15 km (Fu and Ubelmann 2014). With an order of magnitude improvement over the conventional altimeters in two-dimensional coverage, the SWOT mission will not only provide us with finer-resolution mapping of the time-varying SSH field, it will also likely bring about a fundamental change in how we view and comprehend the upper-ocean circulation dynamics on length scales shorter than 200 km.

Concurrent with the development of the SWOT mission, our understanding of the meso- and submesoscale upper-ocean circulation structures has also improved significantly during the last decade. In particular, many investigators have explored the potential of reconstructing three-dimensional (3D) upper-ocean circulation features, including the balanced vertical velocity field, from the information of high-resolution SSH and/or sea surface temperature (SST). One approach for such reconstruction relies on statistical regressions that combine the high-resolution SSH/SST observations with in situ temperature–salinity data to empirically infer the 3D upper-ocean structures. Recent studies utilizing this approach have focused the 3D mesoscale structures of the upper ocean (e.g., Guinehut et al. 2004; Buongiorno Nardelli et al. 2012; Mulet et al. 2012).

The second approach for reconstruction is dynamically based. As detailed in Lapeyre and Klein (2006), the rationale for the dynamical reconstruction stems from the fact that the correlation between the surface and interior potential vorticity (PV) anomalies are the same as that between the large-scale surface and interior PV and that this latter correlation can be deduced from climatological observations. In other words, the upper-ocean circulation structures are reconstructable from the 3D PV inversion with the use of only high-resolution surface information and interior ocean climatology. The simplest approach of dynamical reconstruction is the effective surface quasi-geostrophic (SQG) framework that implicitly takes into account the interior PV through an effective buoyancy frequency (see Lapeyre and Klein 2006). The resulting reconstruction is close to the SQG model with nonzero surface PV and zero interior PV (Blumen 1978; Held et al. 1995). The effective SQG approach has been used for reconstruction of upper-ocean circulation structures by Lapeyre and Klein (2006), LaCasce and Mahadevan (2006), Isern-Fontanet et al. (2006, 2008), Klein et al. (2009), and Smith and Vanneste (2013). More recent advancement relating to the effective SQG reconstruction includes the addition of surface mixed layer parameterizations (Ponte et al. 2013) and the use of both SSH and SST information to constrain the surface and interior PV simultaneously (Ponte and Klein 2013; Wang et al. 2013; Gonzalez-Haro and Isern-Fontanet 2014). For the present study, we choose to use the simple effective SQG framework to test the potential of SWOT observations for the upper-ocean circulation reconstructions.

To examine the validity of the SQG-based dynamics, the investigators listed above have commonly used high-resolution ocean general circulation models (OGCMs) as a test bed either with an idealized model setting or with realistic geometry and external forcings. In such studies, the input data are the OGCM-derived SSH and/or SST fields and the reconstructed upper-ocean circulation structures are quantified by comparing to the modeled "truth" fields. Unlike the model-derived product, SSH data measured by the SWOT satellite will be subject to measurement errors of diverse instrumental and geophysical origins. In addition, the SWOT mission will have a highly irregular sampling pattern in time and space while in its science orbit. In applying the SWOT-derived SSH data to the SQG-based dynamics for reconstructing the 3D upper-ocean circulation features, additional effort is, therefore, needed in assessing the impact of these sampling and measurement errors the input SSH field is subjected to.

The objective of this study is to assess this impact by utilizing the output from a high-resolution North Pacific Ocean OGCM simulation and the recently developed

SWOT simulator. The SWOT simulator is designed to simulate synthetic observations of SSH from the SWOT mission using the SSH field as input of any high-resolution OGCM simulations (Gaultier et al. 2016). It generates the SSH data that have the sampling and error characteristics of the future SWOT mission. A particular issue we are interested in quantifying in this study is the extent to which the SWOT sampling and measurement errors may impact the effective SQG-reconstructed 3D circulation features.

This paper is organized as follows: In section 2, we provide a detailed description for the 1/30°-resolution OGCM for the Earth Simulator (OFES) simulation that serves as the basis of our explorations. After briefly reviewing the effective SQG theory put forth by Lapeyre and Klein (2006) in section 3, we apply the theory to reconstruct the 3D upper-ocean circulation structures in the Kuroshio Extension region. Section 4 provides details about the SWOT simulator and our approach to generate the objectively mapped SSH field. With the use of the objectively mapped SSH field, we examine further in section 4 the reconstructability of the 3D upper-ocean circulation features and quantify the effect due to the SWOT sampling and measurement errors. Section 5 summarizes the findings from the present study and provides perspectives for future explorations.

2. The 1/30°-resolution OFES simulation

The high-resolution OGCM output utilized in this study is the 1/30° OFES simulation run for the North Pacific basin of 20°S–66°N and 100°E–70°W (Sasaki et al. 2014). This simulation uses the global 1/10° OFES simulation output of 1 January 2000 as its initial condition and is forced by the 6-hourly surface wind stress and heat flux data of the Japanese 25-year Reanalysis Project (JRA-25) product (Onogi et al. 2007). The model has 100 levels in the vertical and uses a biharmonic operator for horizontal mixing of momentum and tracers and Noh and Kim's (1999) scheme for vertical mixing. The 1/30° simulation was integrated for 3 yr, and the daily averaged data of SSH, 3D velocity, and temperature–salinity fields in the second and third years (i.e., 2001 and 2002) are used in our following analyses.

To explore the reconstructability of the 3D upper-ocean circulation structures, we will focus throughout this study on the region where the Kuroshio separates from the coast of Japan and enters the deep basin of the North Pacific Ocean (see Fig. 1). Relatively free from the constraint of bathymetry, the Kuroshio Extension (KE) in this segment of the subtropical circulation behaves as an eastward-flowing, inertial jet rich in large-amplitude meanders and energetic pinched-off eddies (see Qiu and Chen 2005 and references therein). By and large, the OFES simulation captures the mean state and the variability of the KE system favorably. For example, Figs. 1a and 1b compare the mean SSH field obtained from the 2-yr OFES simulation with that obtained synergistically from altimetry, gravimetry, and other in situ measurements (see Rio et al. 2014). Both figures reveal that the KE jet has a similar separation latitude near 35°N and is accompanied by two quasi-stationary meanders. In both figures, the two quasi-stationary meanders have their respective southern recirculation gyres. In terms of the simulated versus observed SSH variability, Figs. 1c and 1d also compare well; both figures show high eddy variability in similar geographical locations along the mean KE jet. Notice that the amplitude of the root-mean-square (rms) SSH variability is higher in the simulation than observed, and this is likely a result of AVISO-measured SSH signals capturing only the mesoscale signals with length scales larger than 150 km (Qiu et al. 2014).

Notice that with a 3-km grid resolution in the KE region, the 1/30° OFES simulation captures the eddy variability of length scales similar to that expected to be detected by the SWOT mission (i.e., the eddy variability with a 15-km spectral wavelength scale).

3. Effective SQG and its application to the OFES output

Before addressing the issues of SWOT's spatial–temporal sampling and measurement errors, it is beneficial to assess the extent to which the effective SQG dynamics is able to reconstruct the 3D balanced upper-ocean circulation features in the context of the 2-yr OFES simulation. Specifically, we are interested in the reconstructability of the relative vorticity ζ and vertical velocity w fields in the 1000-m upper ocean given the simulated 1/30° daily mean SSH data.

As expounded in Lapeyre and Klein (2006), the effective SQG dynamics assume that the PV anomalies in the interior upper ocean are correlated to the surface PV (or surface buoyancy) anomalies. Under this assumption, the anomalous geostrophic streamfunction ψ at any upper-ocean depth z is functionally related to the SSH η anomalies via

$$\hat{\psi}(\mathbf{k}, z) = \frac{g}{f_o}\hat{\eta}(\mathbf{k})\exp\left(\frac{N_o}{f_o}kz\right), \tag{1}$$

where the caret $\hat{}$ denotes the horizontal Fourier transform, $\mathbf{k} = (k_x, k_y)$ is the horizontal wavenumber vector, $k = |\mathbf{k}|$, f_o is the Coriolis parameter at a reference latitude (35°N here), g is the gravity constant, and N_o is an

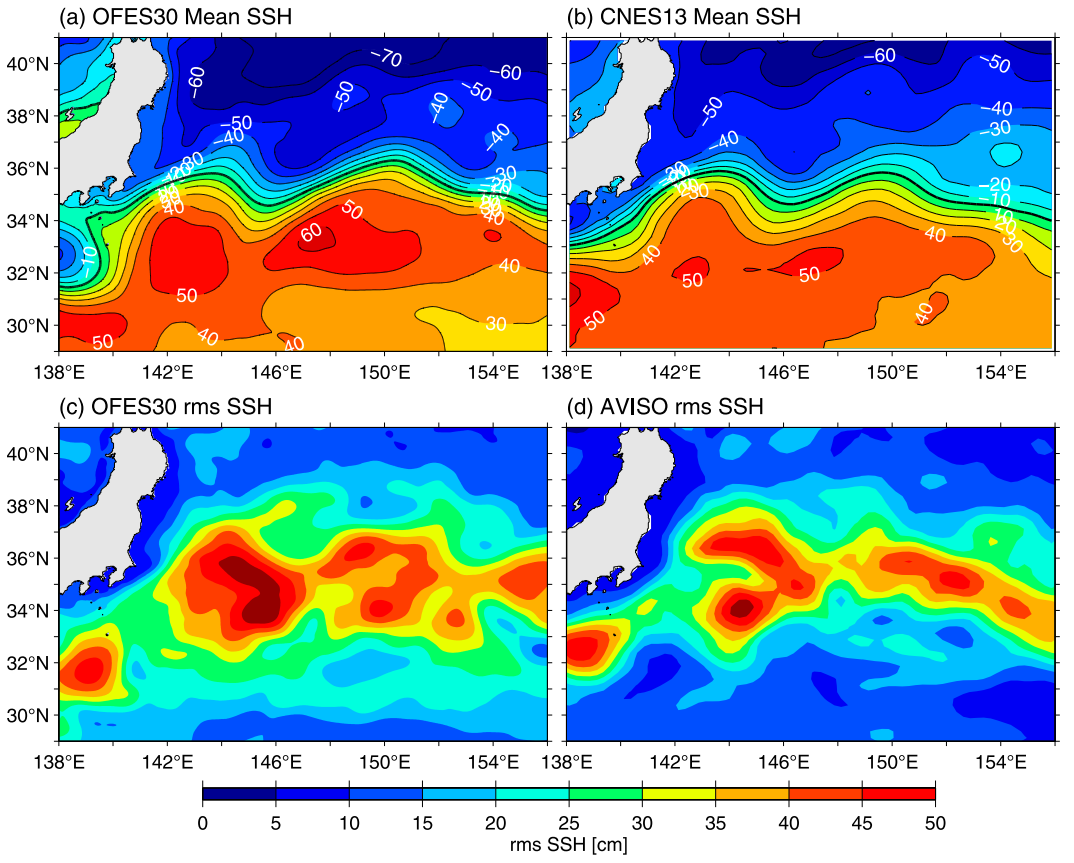

FIG. 1. (a) Mean SSH field in the Kuroshio Extension region from the 2-yr simulation by the 1/30°-resolution OFES model. (b) Mean SSH field derived from the long-term satellite altimetry and in situ measurements by Rio et al. (2014). (c) Root-mean-square SSH variations from the 2-yr simulation by the 1/30°-resolution OFES model. (d) Root-mean-square SSH variations from the satellite altimetry measurements in 2001/02.

"effective" buoyancy frequency that takes into account contributions of the nonzero interior PV signals. Dynamically, Eq. (1) implies that a strong phase relationship exists between the surface and interior dynamical quantities and that this relationship is wavenumber dependent. Once the geostrophic streamfunction is specified, the relative vorticity, buoyancy, and vertical velocity in the upper ocean can be easily deduced through geostrophy, hydrostaticity, and the advective buoyancy equation, respectively:

$$\hat{\zeta}(\mathbf{k}, z) = -k^2 \hat{\psi}(\mathbf{k}, z), \tag{2}$$

$$\hat{b}(\mathbf{k}, z) = \frac{N_o k}{c} \hat{\psi}(\mathbf{k}, z), \quad \text{and} \tag{3}$$

$$\hat{w}(\mathbf{k}, z) = -\frac{c^2}{N_o^2} \left[-\widehat{J(\psi_s, b_s)} \exp\left(\frac{N_o}{f_o} kz\right) + \widehat{J(\psi, b)} \right], \tag{4}$$

where J is the Jacobian operator, and the subscript s denotes the surface value. Notice that Eq. (4) is equivalent to the classical omega equation commonly used to derive the vertical velocity field (Klein and Lapeyre 2009). For the two constants N_o and c in Eqs. (3) and (4), we follow Lapeyre and Klein (2006) and set N_o to correspond to the buoyancy frequency averaged in the upper 300-m layer of the OFES simulation in the KE region of our interest (32°–38°N, 144°–150°E). With this region under strong seasonal surface heat and momentum flux forcing (e.g., Qiu and Kelly 1993), the N_o/f_o value thus determined changes sinusoidally with a minimum of 42 in February and a maximum of 110 in August. In accordance with Klein et al. (2009), $c = 1.6$ is chosen such that the rms amplitude of the reconstructed w matches that in the OFES simulation.[1]

To apply the effective SQG method for reconstruction in the KE region of 32°–38°N and 144°–150°E, we use the OFES SSH data $\eta(x, y, t)$ in a larger box of 30°–40°N and 142°–152°E as input. Our selection of a 6° × 6° box for

[1] During the future SWOT mission, the N_o value can be evaluated by in situ temperature–salinity measurements from, for example, the global Argo array and the c value by concurrent satellite SSH and SST measurements with the use of Eq. (3) at $z = 0$.

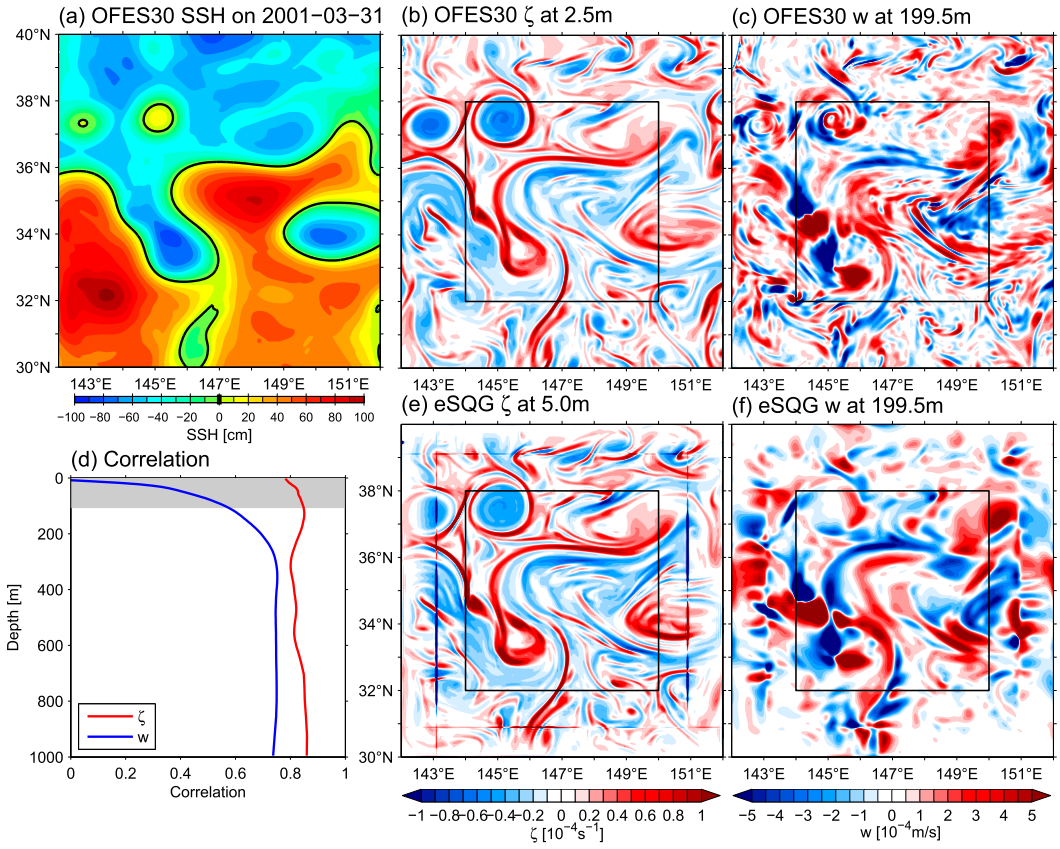

FIG. 2. (a) OFES SSH input field from reconstruction on 31 Mar 2001. (b) Relative vorticity ζ at 2.5 m and (c) vertical velocity w at 199.5 m from the OFES simulation on 31 Mar 2001. (e) ζ at 5.0 m and (f) w at 199.5 m reconstructed based on the effective SQG theory. (d) Linear correlation coefficients for ζ (red line) and w (blue line) between the original and reconstructed fields as a function of depth. Gray shade denotes the mixed layer depth averaged in the reconstruction region of 32°–38°N and 144°–150°E.

reconstruction is determined by the need for manageable objective interpolation of the SSH field (to be discussed in the appendix later) and the dynamical constraint that reconstruction for w requires a broad spatial domain that resolves the buoyancy advection by mesoscale eddy flows. As an example, Fig. 2a shows the OFES SSH field in this 10° × 10° box for 31 March 2001. In this SSH snapshot, the trough of the KE's first quasi-stationary meander near 146°E is seen to extend southeastward just before the cutoff of a cold-core ring. At the same time, a cold-core ring developed from the trough of the KE's second quasi-stationary meander is seen to appear near 150°E. Very similar KE meandering patterns and cold-core rings have been detected by satellite altimetry measurements (see, e.g., Fig. 3 in Qiu et al. 2007). To derive the $\hat{\psi}(\mathbf{k}, z)$ field in Eq. (1), we first remove the large-scale SSH signals through the bilinear least-squares fitting and then apply the 2D trapezoid windowing to the 1° band along the box edges. Once $\hat{\eta}(\mathbf{k})$ is obtained by the Fourier transform, the 3D vorticity and vertical velocity fields can be readily reconstructed through Eqs. (2) and (4) via the inverse Fourier transform. To avoid the edge effect, our comparison below between the simulated and reconstructed fields will be conducted in the 32°–38°N and 144°–150°E box of our initial selection.

Figure 2e shows the near-surface relative vorticity ζ field reconstructed using Eq. (2). Compared to the simulated ζ field shown in Fig. 2b, there is a clear visually favorable correspondence between the reconstructed and the targeted fields. The linear correlation coefficient between Figs. 2b and 2e reaches 0.79. As indicated in Fig. 2d by the red line, the pattern correlation between the reconstructed and simulated ζ fields remains at the 0.8 level throughout the upper 1000-m layer. This comparison confirms the findings by previous studies that in the absence of errors in the input SSH field, the effective SQG theory constitutes a useful method for 3D reconstruction of the upper-ocean relative vorticity field.

For comparison, Figs. 2c and 2f show the simulated and reconstructed w fields, respectively, at 200-m depth. The

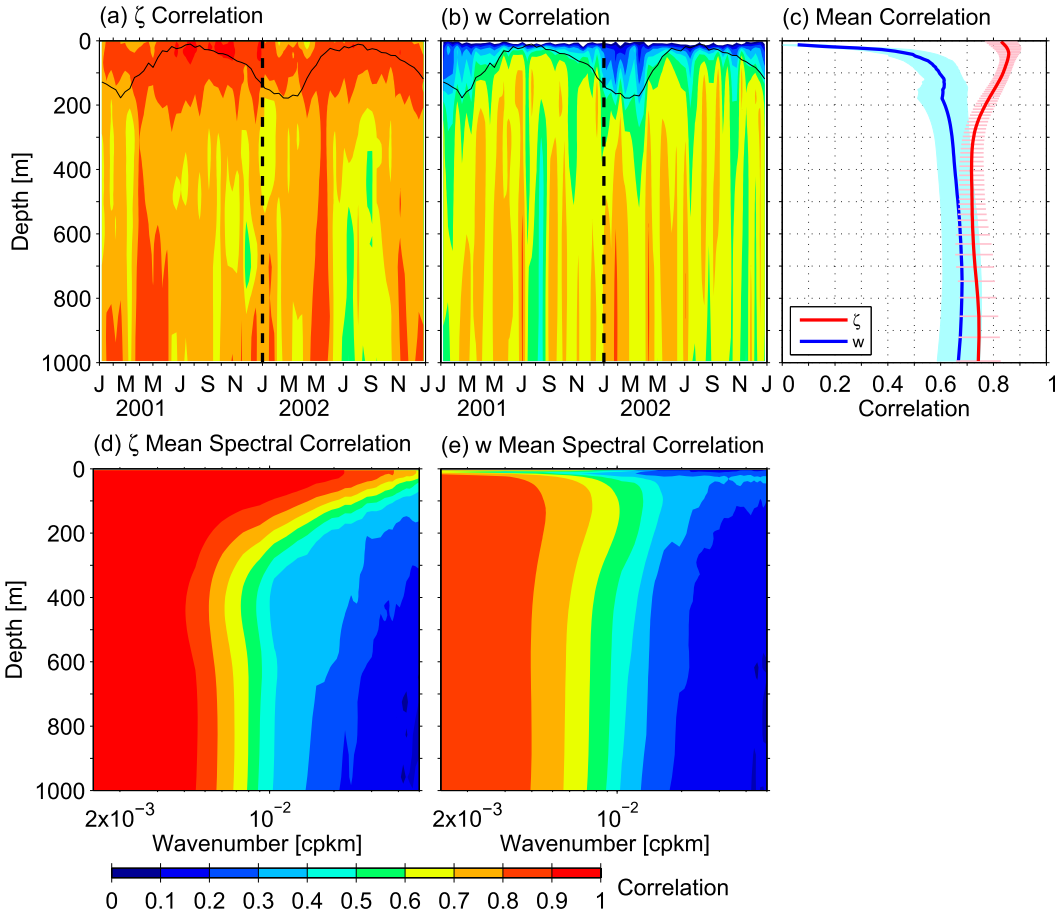

FIG. 3. (a) Linear correlation coefficient between the original and reconstructed ζ fields as a function of time and depth. (b) As in (a), but for the w fields. In (a) and (b), solid black lines denote the mixed layer depth averaged in the reconstruction region of 32°–38°N and 144°–150°E, and black dashed lines denote the beginning of 2002. (c) Linear correlation coefficient for ζ (red line) and w (blue line) averaged in 2001/02. Horizontal bars denote the standard deviations. (d) Spectral correlation averaged in 2001/02 between the original and reconstructed ζ fields as a function of horizontal wavenumber and depth. (e) As in (d), but for the w fields.

reconstructed w captures much of the mesoscale signals but fails to recover the smaller-scale features [i.e., with length scales $< O(50)$ km] embedded in the mesoscale signals. The linear correlation coefficient between Figs. 2c and 2f is 0.70. Because the submesoscale signals in the region are caused by the frontal instability of the KE jet and their magnitudes tend to diminish with depth (Sasaki et al. 2014), the pattern correlation between the simulated and reconstructed w fields has a generally increasing tendency with depth in the upper 300-m layer (see the blue line in Fig. 2d). The gray shading in Fig. 2d shows the ML depth averaged in our reconstruction box of 32°–38°N and 144°–150°E. Here, the ML depth is defined as where the water density becomes $0.125\,\mathrm{kg\,m^{-3}}$ larger than the surface density. As the vertical velocity within the ML can be dictated by turbulent eddy mixing, the process unrepresented in Eq. (4), the correlation coefficient for the simulated and reconstructed w is generally low (<0.6) within the surface ML. In considering this deficiency of the effective SQG theory, we will focus on the reconstructability of w below the box-averaged ML depth in our following analyses.

It is important to note that the results presented in Fig. 2d are typical of the correlations obtained for ζ and w throughout the 2-yr OFES simulations. Figures 3a and 3b show the correlations between the simulated and reconstructed ζ and w fields, respectively, as a function of time and depth. Averaged over the 2 yr, the correlation for ζ (red line in Fig. 3c) generally exceeds 0.8 in the upper 200-m layer and falls in between 0.7 and 0.8 below 200 m. For the w field averaged over the 2 yr below the ML depth (blue line in Fig. 3c), the correlation falls by and large in between 0.6 and 0.7, except within the surface layer shallower than 100 m.

In addition to the correlation based on the real-valued ζ and w fields, it is also possible to evaluate the

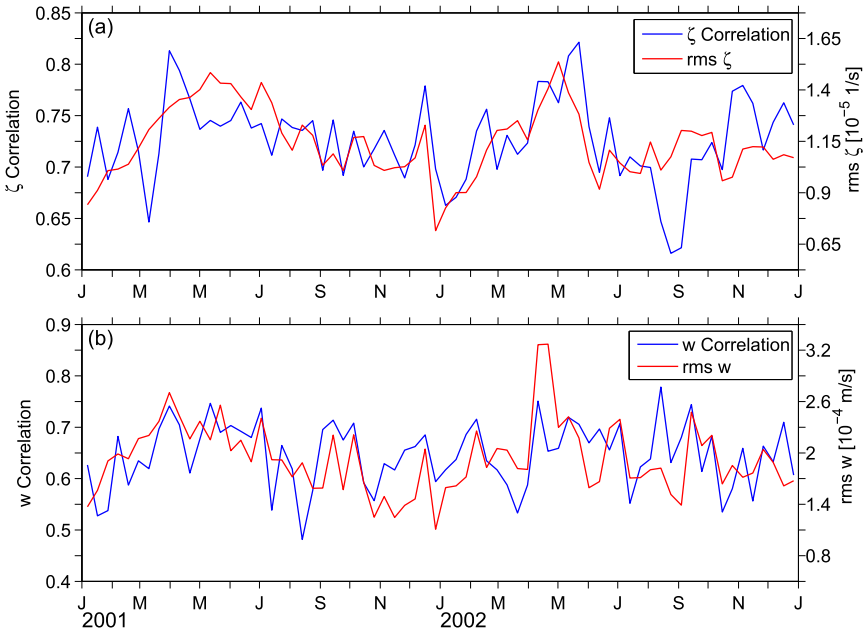

FIG. 4. (a) Blue line indicates the time series of correlation coefficient between the simulated and reconstructed ζ averaged in the 200–500-m layer. Red line indicates the time series of rms ζ value averaged in the 200–500-m layer of the OFES simulation. The two time series have a linear correlation coefficient 0.48. (b) As in (a), but for the w field. The two time series has a linear correlation coefficient 0.46.

scale-dependent correlation in the spectral space. Figures 3d and 3e show the spectral correlation averaged in 2001/02 between the original and reconstructed ζ and w fields, respectively, as a function of horizontal wavenumber and depth. For both fields, the effective SQG theory achieves a better reconstruction for the mesoscale signals than for the submesoscales. For the w field, for example, the spectral correlation in general exceeds (falls below) 0.5 for signals with a wavelength longer (shorter) than 100 km. For the ζ field, on the other hand, there is a tendency for the spectral correlation to improve toward the surface ocean (e.g., the near-surface spectral correlation for ζ can reach 0.9 at wavelengths as short as 50 km).

A closer look at Figs. 3a and 3b reveals that although the regional ML depth undergoes a regular seasonal cycle (see the black lines in Figs. 3a and 3b), seasonal variability appears less prominent in the correlation time series between the simulated and reconstructed ζ and w fields. By examining the time-varying relative vorticity and vertical velocity fields in the OFES simulation, we find that the amplitude of the correlation coefficient for both ζ and w tends to depend on the rms amplitude of the original ζ and w field. As shown in Figs. 4a and 4b, which compare the linear correlation coefficient time series with the rms amplitude time series for ζ and w, a larger rms amplitude in the original ζ and w field usually results in a better reconstruction of the targeted ζ and w field. Dynamically, this makes sense because the 3D reconstruction of the effective SQG theory relies on the subtle and spatially distorted SSH features. The greater the amplitude in SSH signal, the more successful the reconstruction.

4. SWOT simulator and its application to the OFES output

As noted in the introduction, the SWOT simulator is designed to be applied to OGCMs, such as the $^1/_{30}°$-resolution OFES simulation, for the exploration of ideas and methods to optimize the information retrieval from the SWOT mission. From the OGCM SSH input, the simulator generates SWOT-like output on a swath along the orbit ground track and adds measurement errors and noise according to the specifications by the SWOT project team (Gaultier et al. 2016). The swath has a width of 120 km and a nadir gap of 20 km. Within each swath, the output SSH field has a 2-km along- and across-track resolution. During its science orbit, the SWOT satellite will have a 20.86-day repeat cycle; with an inclination at 77.6° latitude and an altitude of 891 km, it can cover the global ocean in 292 passes in a repeat cycle.

For the 6° × 6° box in the KE region of our interest, Fig. 5 shows that the SWOT measurements within the 20.86-day repeat cycle can be temporally grouped into two subcycles. In each subcycle, the time difference among the neighboring tracks is less than ±2 days. In addition to the 20-km nadir gaps along the swaths, there also exist diamond-shaped gaps in between the juxtaposed swaths within a subcycle (see Fig. 5a). Spatially, these diamond-shaped gaps are filled by the swaths from the other subcycle separated by about 10 days (cf. Fig. 5b). Using the daily OFES SSH data as input, Fig. 6a shows the SSH field in a subcycle centered on 31 March 2001, generated by the SWOT simulator. Compared to the OFES-simulated SSH field on 31 March, shown in Fig. 2a, it is clear that SSH discontinuities appear along the swath edges due to the difference in sampling times. Figure 6b shows the simulator-generated SSH field after the expected SWOT measurement errors (shown in Fig. 6c) have been added. As detailed in Gaultier et al. (2016), the measurement errors have all spatial scales, but they tend to exert more impact on smaller-scale SSH signals because of the larger noise-to-signal ratios.

For comparison, Fig. 6d shows the simulator-generated SSH field centered on 10 April 2001, 10 days (or a subcycle) after Fig. 6a. Notice that although the diamond-shaped gaps in Fig. 6a are filled by the SSH measurement in this succeeding subcycle, the SSH field can, however, evolve drastically within a 10-day period. For example, the large-amplitude trough of the first quasi-stationary meander seen near 145°E in Fig. 6a became a cutoff cold-core ring in Fig. 6d. As such, in addition to the instrumental/geophysical errors associated with the SWOT measurement, the irregular temporal and spatial sampling along the swaths introduces another source of input SSH errors that need to be contended with in applying the effective SQG theory for reconstruction of the 3D upper-ocean circulation field.

To minimize these measurement and sampling errors, we utilize the objective interpolation method to convert the simulator-generated SSH output field (i.e., those shown in Figs. 6b and 6e) into the regular 10° × 10° SSH field centered on a given date for reconstruction. Detailed formulations regarding the objective interpolation method are given in the appendix. As an example, we show in Fig. 7a the objectively mapped SSH field centered on 31 March 2001. Compared to the original SSH field simulated by OFES shown in Fig. 2a, it is clear that mesoscale features associated with the unstable KE jet are mostly captured in Fig. 7a. The pattern correlation coefficient between Figs. 2a and 7a is as high as 0.96. While similar in spatial pattern, it is also discernible from comparison that the SSH variability in the objectively mapped field has a more reduced amplitude than the simulated field and that many of the finescale SSH features have been smeared out. Regressing the mapped SSH field against the original SSH field reveals that the signal variance after objective mapping[2] is reduced by $r = 9.7\%$.

Using the objectively mapped SSH field of Fig. 7a as input, we plot in Figs. 7c and 7d the near-surface ζ and 200-m w fields reconstructed from the effective SQG theory. Because of the temporal and spatial smoothing to the input SSH field, the reconstructed ζ and w exhibit spatially blurred patterns when compared to the ζ and w reconstructed based on the original SSH data (recall Figs. 2e,f). Despite this loss in sharpness, the spatial patterns of ζ and w are nevertheless adequately reproduced in Figs. 7c and 7d. In terms of the correlation coefficient between the reconstructed and simulated fields in the upper water column (Fig. 7b), the ζ field remains in the 0.7–0.85 range. Averaged vertically, this corresponds to a 0.04 reduction only in respect to the ζ correlation shown in Fig. 2d. Regarding the w field, the correlation below the ML depth falls in between 0.4 and 0.6. This corresponds to a larger, 0.18 reduction in respect to the w correlation obtained by using the original SSH field (cf. the blue line in Fig. 2d).

The fact that the reconstruction of vertical velocity is more sensitive to the temporal and spatial smoothing of the SSH field is because of the different decorrelation time scales in the ζ versus w fields. Figure 8a shows the autocorrelation as a function of time for the 2-yr OFES-simulated ζ and w fields in the upper-ocean (0–500 m) KE region of 32°–38°N and 144°–150°E. Compared to the 5.5-day integral time scale for the ζ field, the integral time scale for w is only 1.5 days. Interestingly, the spatial decorrelation scales for ζ and w fields in the upper-ocean KE region are nearly identical at about 8 km (Fig. 8b). It is, thus, the shorter temporal decorrelation scale that causes the reconstructed w field to degrade more severely than the ζ field when the SWOT sampling and measurement errors are taken into account in their reconstructions.

To evaluate the impact on the reconstruction based on the objectively mapped SSH data more robustly, we apply the SWOT simulator to the 2-yr output of the OFES simulation (corresponding to 70 subcycles of the SWOT mission) and compare the resulting reconstructed ζ and w fields with those based on the input of the original SSH data. Figure 9 shows the results similar to those shown in Fig. 3 except the input SSH field in this case is that sampled by the SWOT simulator, including the

[2] Specifically, $r = \langle [h_s(x,y) - h_o(x,y)]^2 \rangle / \langle h_s^2(x,y) \rangle$, where h_o denotes the objectively mapped SSH field, h_s the simulated SSH, and $\langle\ \rangle$ the spatial ensemble average.

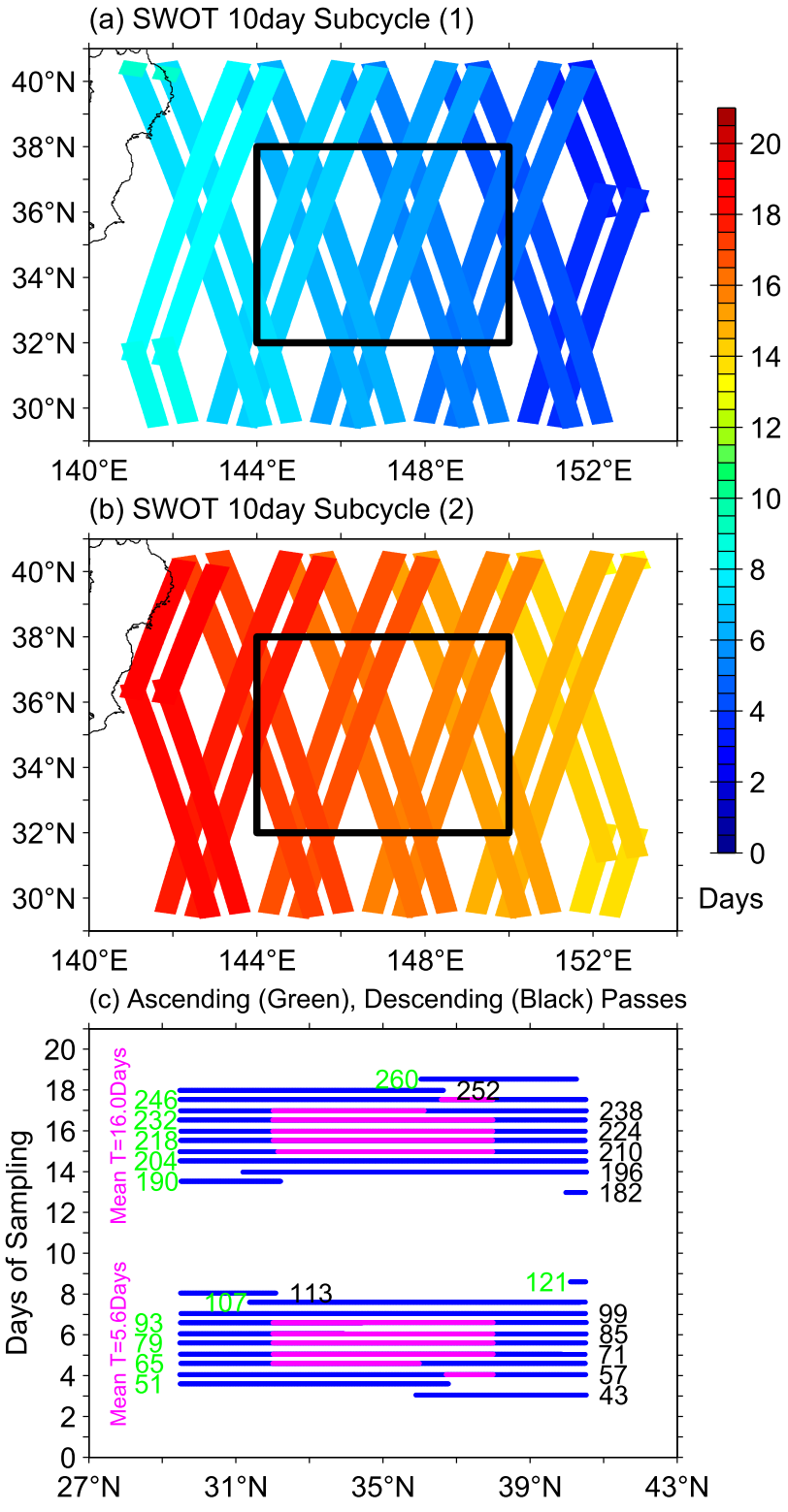

FIG. 5. Spatial swath distributions during the 21-day repeat cycle of the SWOT mission in the KE region east of Japan: (a) the first vs (b) the second subcycle. Colors denote the days within the 21-day repeat cycle. (c) Swath passes in the KE region (blue lines) as a function of time and latitude. Pink lines denote the pass segments that fall in the 32°–38°N and 144°–150°E box.

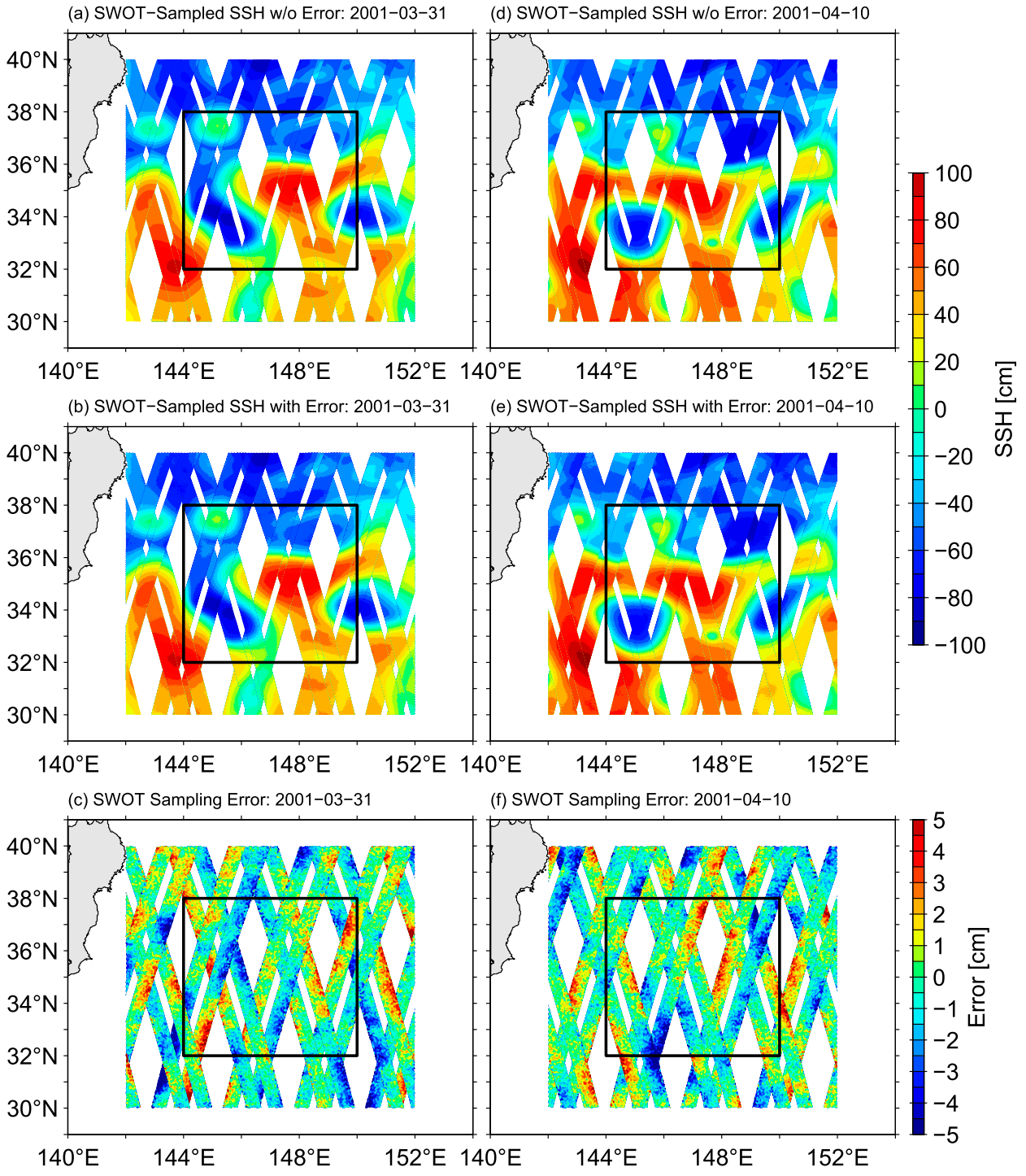

FIG. 6. Along-swath (a) OFES SSH and (c) measurement error data generated by the SWOT simulator within the subcycle centered on 31 Mar 2001. (b) The along-swath SSH data with the measurement errors added. Notice the difference between the color scales for (a) and (b) vs (c). (d)–(f) As in (a)–(c), but for the subsequent subcycle centered on 10 Apr 2001.

measurement errors, and objectively mapped in space and time. Consistent with the case shown above for 31 March 2001, degradation in ζ reconstruction due to the sampling and measurement errors is relatively small. Compared to 0.7–0.85 indicated by the red line in Fig. 3c, the range for ζ correlation in Fig. 9c is 0.68–0.75. In the spectral domain, a visual comparison between Figs. 3d and 9d indicates that the degradation in ζ correlation

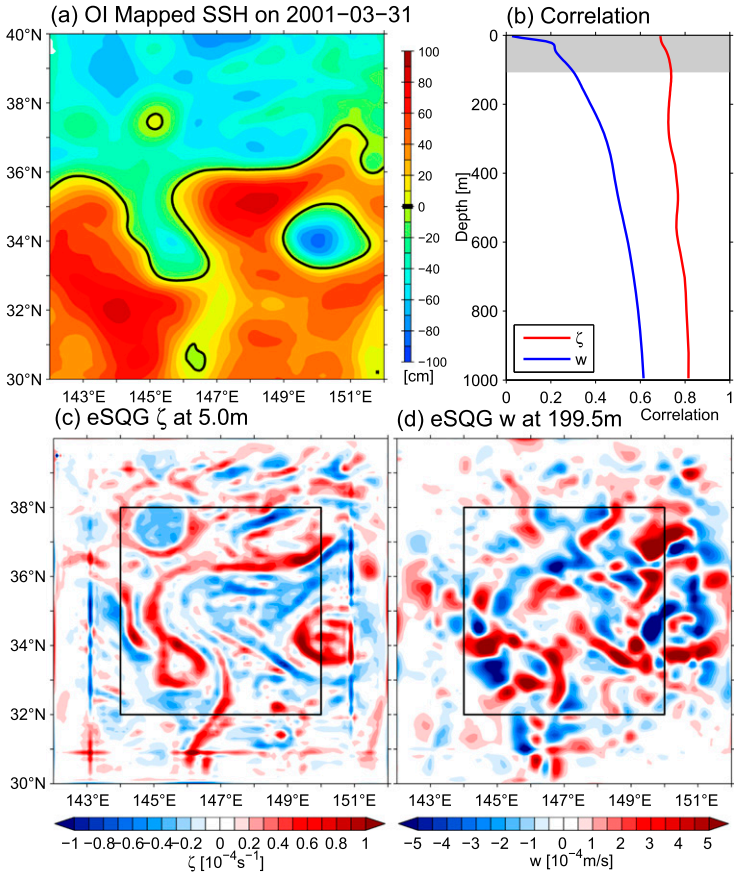

FIG. 7. (a) Objectively mapped SSH field centered on 31 Mar 2001, based on the SWOT simulator sampled SSH data shown in Fig. 6b. (c),(d) ζ at 5.0 m and w at 199.5 m reconstructed based on the effective SQG theory using (a) as the input SSH field. (b) Linear correlation coefficients for ζ and w between the original (those shown in Figs. 2b,c) and reconstructed fields as a function of depth. Gray shade denotes the mixed layer depth averaged in the reconstruction region of 32°–38°N and 144°–150°E.

occurs across the entire wavenumber space. In addition, there appears a hint that the degradation is more severe in the surface layer than at depth.

To evaluate the depth-dependent degradation in correlation more quantitatively, we plot in Fig. 10b (red line) the relative ratio:

$$r(z) = [r_s(z) - r_o(z)]/r_s(z), \tag{5}$$

for ζ as a function of depth, where $r_s(z)$ is the correlation (in real space) based on the simulated SSH input and $r_o(z)$, the objectively mapped SSH input (i.e., the red solid and dashed lines in Fig. 10a). The relative degradation is about 17% in the surface layer and drops to ~5% below 500-m depth. These values confirm that the impact due to the SWOT sampling and measurement errors will likely be small for the 3D ζ reconstruction.

As we have emphasized for the case of 31 March 2001, the degradation for w reconstruction is more severe than that for ζ reconstruction. Figure 9c reveals that the 2-yr-averaged w correlation has a range of 0.4–0.6 as compared to 0.5–0.7 in Fig. 3c (also shown as blue lines in Fig. 10a). In the spectral domain (Fig. 9e), the correlation degradation in w also occurs across the entire wavenumber space. Compared to Fig. 3e, for example, the spectral correlation boundary of 0.5 shifted from the $O(100)$ km wavelength in Fig. 3e to $O(130)$ km in Fig. 9e. Finally, in terms of the degradation ratio defined in Eq. (5), $r(z)$ for w falls in the 15%–25% range (the blue line in Fig. 10b). This suggests that while more prone to the sampling and measurement errors, the SQG-reconstructed w information will, nevertheless, be useful in inferring the upper-ocean vertical motions in strong western boundary current regions from the planned SWOT mission.

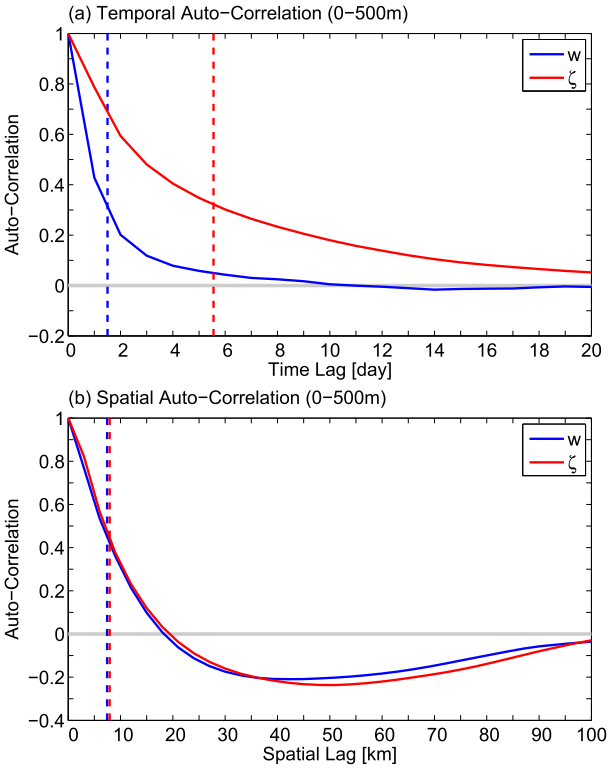

FIG. 8. (a) Temporal autocorrelation functions (solid lines) for the 2-yr simulated ζ and w field in the upper-ocean (0–500 m) KE region of 32°–38°N and 144°–150°E. Dashed lines denote the integral time scales defined by $I = \int_0^{T_o} c(t)\,dt$, where $c(t)$ is the autocorrelation and T_o is its first zero-crossing (Stammer 1997). (b) As in (a), but for the spatial autocorrelation functions.

5. Summary and discussion

In preparation for the launch of the SWOT satellite in 2020, the present study explored the reconstructability of the upper-ocean structures with the use of the SWOT interferometer-derived swath SSH information. Our explorations utilized the 1/30°-resolution North Pacific OFES OGCM output to represent the time-evolving oceanic state. As shown by Sasaki et al. (2014) and Qiu et al. (2014), this OGCM simulation captured a strong impact of submesoscales upon the upper-ocean dynamics. An original aspect of the present study is the use of the SWOT simulator tool that mimics the temporal and spatial sampling of the SWOT satellite and generates instrumental and geophysical errors expected for the SWOT measurements. The specific oceanic variables that we have focused on were the 3D relative vorticity and vertical velocity fields, and it is important to emphasize that reconstructing the vertical velocity is a real challenge since it depends not only on the second-order derivatives of SSH, but also on the phase relationship between the SSH derivatives with those of the density field.

The success of reconstructing the upper ocean ζ and w fields from the SWOT mission depends on two important procedures: The first is the theoretical framework on which the 3D reconstruction is based, and the second is the procedure that minimizes the sampling and measurement errors intrinsic to the SWOT mission. For the theoretical framework, the present study adopted the simple effective SQG theory proposed by Lapeyre and Klein (2006). For the Kuroshio Extension region considered in our study, the effective SQG theory was found to be a functioning and beneficial framework. Specifically, averaging over the 2-yr OFES simulation period, the correlation between the SQG-reconstructed and simulated ζ field is as high as 0.7–0.85 in the upper 1000-m layer. The correlation for the w field is also high below the mixed layer, ranging from 0.6 to 0.7 in the 100–1000 layer. Fixed in time, there exists a trend that the reconstruction for ζ and w improves if the spatial eddy variability is enhanced.

To reduce the sampling and measurement errors associated with the SWOT mission, we devised in this study an objective interpolation scheme that converts the large, irregularly sampled, swath SSH data into a spatially regular grid suitable for reconstruction. The impact due to the SWOT sampling and measurement errors was estimated to be small for the ζ reconstruction. Averaged over the 2-yr OFES simulation period, degradation for the reconstructed ζ using the objectively mapped SSH input data has a 5%–15% ratio relative to the reconstructed ζ based on the simulated SSH input data. With respect to the reconstructed w field below the mixed layer, the degradation due to the SWOT sampling and measurement errors is more severe, and the relative ratio is in the range of 15%–25%. It is worth emphasizing that there exists at present no reliable means to measure the vertical motions in the global oceans (e.g., Rudnick 1996). As such, although less accurate than the reconstructed ζ structures, we believe the 3D w field reconstructed from the SWOT mission will constitute, nevertheless, a valuable product for physical and interdisciplinary oceanographic studies.

The reconstruction region chosen for this study is located in the upstream Kuroshio Extension where the mesoscale eddy variability is most active in the Pacific Ocean basin (e.g., Chelton et al. 2011). Indeed, as indicated in Fig. 11, the Rossby number (defined as the ratio of surface rms ζ over f) averaged in region 1 from the 2-yr OFES simulation reaches $R_o = 0.32$. While exploring the reconstructability of ζ and w over the entire North Pacific basin is beyond the scope of this study,

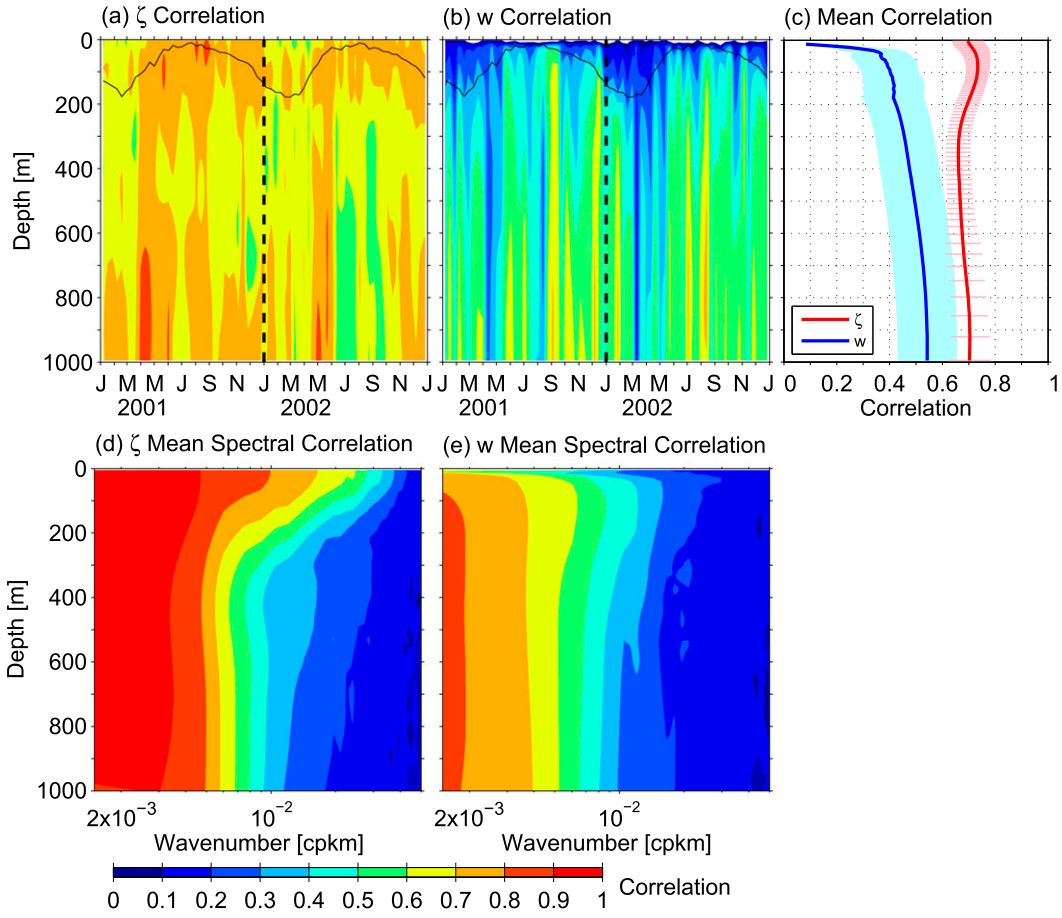

FIG. 9. As in Fig. 3, but the input SSH data for reconstruction is sampled by the SWOT simulator with the expected measurement errors added. It is further objectively mapped in time and space.

we did extend our analyses to the three downstream regions along the Kuroshio Extension path.[3] In regions 2, 3, and 4, shown in Fig. 11, the region-averaged Rossby number becomes progressively smaller from $R_o = 0.25$ to 0.22 to 0.16 (in terms of the rms surface velocity, the four regions have an amplitude of 0.45, 0.36, 0.29, and 0.18 m s^{-1}, respectively). In Figs. 10c, 10e, and 10g, we plot the 2-yr-averaged correlations between the simulated and reconstructed ζ (red) and w (blue) fields. Here, the reconstructed results using the original SSH data as input are shown by solid lines, and those using the objectively mapped SSH data as input are shown by dashed lines. Similar to Fig. 10b for the upstream Kuroshio Extension region, the relative degradation ratios for ζ and w in regions 2, 3, and 4 are plotted in Figs. 10d, 10f, and 10h, respectively.

For the 3D ζ reconstructions based on the original SSH data, a comparison among the red solid lines in the left column of Fig. 10 reveals that there exists no obvious dependence on the regional R_o value; the effective SQG theory performs similarly well independent of the level of regional eddy variability. On the other hand, the ζ reconstructability in the case of using the SWOT-measured SSH data tends to degrade more severely in regions with a smaller R_o value (cf. the red lines in the right column of Fig. 10). Physically, this is understandable because as the regional eddy variability weakens, the SWOT sampling and measurement errors become relatively more pronounced, resulting in a less accurate ζ reconstruction.

With regard to the w reconstructions based on the original SSH data, the blue solid lines in the left column of Figs. 10a, 10c, and 10e reveal that the correlation to the simulated w field is a weak function of R_o and falls in the 0.6–0.7 range. The correlation for w does, however, drop significantly in region 4 where the regional Rossby number falls below 0.2. For the same reason of

[3] Strictly speaking, the eastern edge of the Kuroshio Extension is commonly defined along the date line, and region 4 falls in the domain of the North Pacific Current.

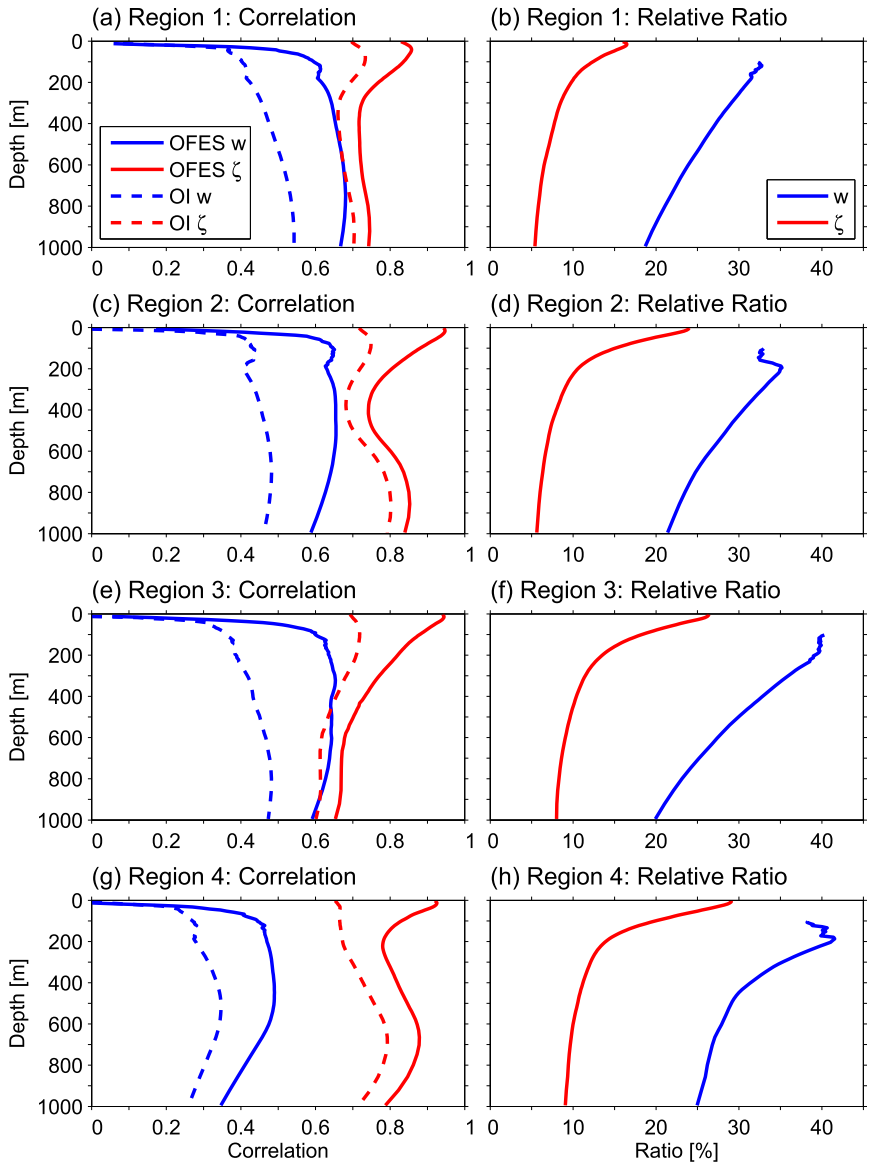

FIG. 10. (a) Correlations between the simulated and reconstructed ζ and w fields in region 1 of the Kuroshio Extension (see Fig. 11). Reconstructed results using the original (objectively mapped) SSH data as input are shown by solid (dashed) lines. (b) Relative degradation ratios for ζ and w as defined by Eq. (5). To avoid the seasonally evolving ML effect, the ratio for w is evaluated only below 100 m. (c)–(h) As in (a) and (b), but for regions 2, 3, and 4, respectively.

signal-to-noise ratio we noted above, the relative degradation ratio for w generally worsens as the regional R_o drops (cf. the blue lines in the right column of Fig. 10).

Three points are worth remarking in concluding this study: First, the OFES simulation that formed the basis of our analyses does not include tidal forcing. This prevented us from examining the extent to which the internal tide signals, which will be present in the SWOT SSH measurements, can impact our reconstruction of the balanced ζ and w fields. For the Kuroshio Extension region with a high level of mesoscale eddy variability, a recent study by Richman et al. (2012) found that the internal tide signals should not distort significantly the SSH signals in the 70–250-km wavelength range. In other words, the internal tide impact upon the reconstruction results presented in this study is likely to be small. To verify this conjecture, however, future studies that can quantify the surface tide and wave effects are desired.

Second, there is a need to improve the effective SQG framework that formed the foundation for our 3D reconstruction. In particular, the effective SQG

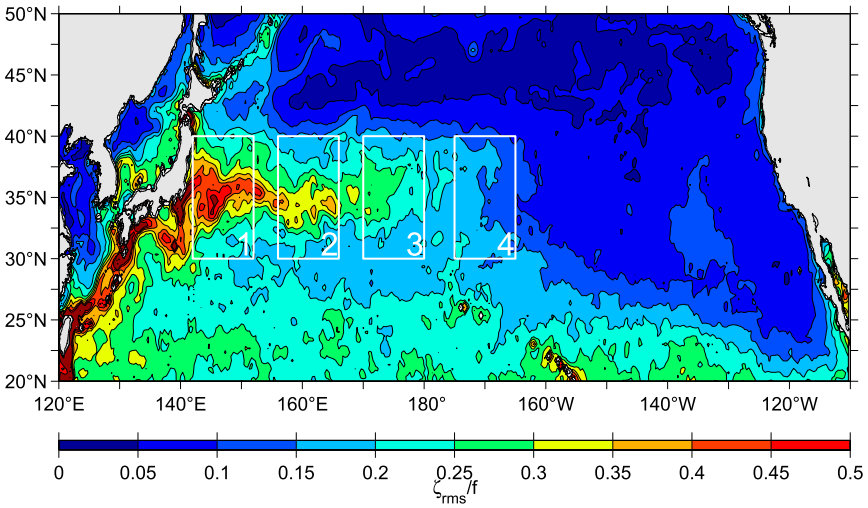

FIG. 11. Distribution of the ratio of surface rms ζ over f, or the Rossby number R_o, from the 2-yr OFES simulation. Region 1 denotes the upstream Kuroshio Extension and forms the main focus of our analyses. Regions 2, 3, and 4 are in the downstream Kuroshio Extension with progressively lower R_o values.

theory does a poor job of reproducing the w field in the surface mixed layer. Some progress in addressing this problem has been made recently by Ponte et al. (2013) by adding the turbulent mixing effect to the effective SQG formulations. In addition to the SSH information, several investigators have also advocated to include concurrent SST information to better constrain the surface and interior PV fields for the 3D reconstruction (Ponte et al. 2013; Ponte and Klein 2013; Wang et al. 2013; Gonzalez-Haro and Isern-Fontanet 2014). Clearly, there is room for improvement in the theoretical framework, and future effort is called for to pursue this.

Third, our adopted objective mapping approach to reduce the measurement errors and to convert the irregular swath SSH data to a regular grid is statistical by nature. Because of the wide gaps between the neighboring swaths, the objectively mapped SSH field is necessarily smoothed, and this impacts negatively on the ζ and w reconstructions due to their dependence on high-order derivatives of the input SSH field. Rather than relying on statistical approaches, Ubelmann et al. (2015) have recently proposed a covariance model that takes into account the nonlinearities of the first baroclinic mode evolution of the SSH field. By filling the swath gaps dynamically, this approach preserves some of the temporally evolving, small-scale, SSH features and is capable of potentially improving the 2D mapping of the SSH field needed for reconstructions. We plan to adopt this approach in our follow-up analyses to this study.

Acknowledgments. We thank Rosemary Morrow and Dudley Chelton for fruitful discussions. Constructive comments made by two anonymous reviewers helped improve an early version of the manuscript. B. Q. and S. C. acknowledge support from NASA SWOT and OSTST missions (NNX13AD91G and NNX13AE51E). P. K. acknowledges the support of CNRS (France) and Agence Nationale pour la Recherche [ANR-09-BLAN-0365-02 (REDHOT) and ANR-10-LABX-19-01 (LabexMER)]. C. U. and L. F.'s research presented in this paper was carried out in part at the Jet Propulsion Laboratory, California Institute of Technology, under contract with the National Aeronautic and Space Administration. They acknowledge support from the SWOT projects. H. S. is supported by MEXT/JST KAKENHI 25400473. The OFES simulation was conducted by using the Earth Simulator under support of JAMSTEC and the Canon Foundation.

APPENDIX

Objective Interpolation of the Simulator-Generated SSH Field

Let r_n ($n = 1, 2, \ldots, N$) be the mapped SSH grid for reconstruction and r_m ($m = 1, 2, \ldots, M$) be the SWOT simulator output positions in both space and time. In our present study, r_n is the regular $0.1° \times 0.1° \times 1$ day grid in the KE region of 30°–40°N and 142°–152°E (Fig. 2a), and r_m is the SWOT measurement points with a 2-km resolution along and across the juxtaposed swaths (Fig. 6).

Within a subcycle in the 10° × 10° box of our interest, the size for N is 101 × 101 × 7 = 71 407, and the size for M is about 3×10^5. The optimal interpolation method minimizes the variance of the SSH estimate $h(r_n)$ from its true value at each r_n, provided that we know the $N \times M$ covariance matrix $\mathbf{R}_{hd}$ between $h(r_n)$ and the observations $d(r_m)$ and the $M \times M$ covariance matrix $\mathbf{R}_{dd}$ among the observations $d(r_m)$. By denoting $\mathbf{h}$ as $h(r_n)$ and $\mathbf{d}$ as $d(r_m)$, the objectively interpolated $\mathbf{h}$ field is given by

$$\mathbf{h} = \mathbf{R}_{hd}\mathbf{R}_{dd}^{-1}\mathbf{d} \tag{A1}$$

(Wunsch 1996). However, this formula is undesirable for a densely sampled system like SWOT because one has to invert the very large $M \times M$ matrix $\mathbf{R}_{dd}$. To make the problem more tractable, we follow Wunsch (1996) and assume the following linear relationship between $\mathbf{h}$ and $\mathbf{d}$:

$$\mathbf{E}\mathbf{h} + \boldsymbol{\epsilon} = \mathbf{d}, \tag{A2}$$

where each row of $\mathbf{E}$ is the linear interpolation of h to each point in $\mathbf{d}$, and $\boldsymbol{\epsilon}$ represents the expected measurement errors specified by the SWOT simulator. Assuming $\boldsymbol{\epsilon}$ is uncorrelated with $\mathbf{h}$, we then have $\mathbf{R}_{hd} = \mathbf{R}_{hh}\mathbf{E}^{\mathrm{T}}$ and $\mathbf{R}_{dd} = \mathbf{E}\mathbf{R}_{hh}\mathbf{E}^{\mathrm{T}} + \mathbf{R}_{\epsilon\epsilon}$, where $\mathbf{R}_{\epsilon\epsilon}$ is the noise covariance matrix and is diagonal: $\sigma_\epsilon^2\mathbf{I}$. By adopting Eq. (A2), Eq. (A1) becomes

$$\mathbf{h} = \mathbf{R}_{hh}\mathbf{E}^{\mathrm{T}}(\mathbf{E}\mathbf{R}_{hh}\mathbf{E}^{\mathrm{T}} + \mathbf{R}_{\epsilon\epsilon})^{-1}\mathbf{d}, \tag{A3}$$

which can be rearranged as

$$\mathbf{h} = (\mathbf{R}_{hh}^{-1} + \mathbf{E}^{\mathrm{T}}\mathbf{R}_{\epsilon\epsilon}^{-1}\mathbf{E})^{-1}\mathbf{E}^{\mathrm{T}}\mathbf{R}_{\epsilon\epsilon}^{-1}\mathbf{d}, \tag{A4}$$

where $\mathbf{R}_{\epsilon\epsilon}^{-1} = 1/\sigma_\epsilon^2\mathbf{I}$. Unlike Eq. (A1), we need only to invert the $N \times N$ matrix twice to obtain $\mathbf{h}$ based on Eq. (A4).

In this study, $\mathbf{R}_{hh}$ is given by the autocovariance function:

$$C(r,t) = \sigma_h^2\left[1 + \frac{r}{L_{xy}} + \frac{1}{6}\left(\frac{r}{L_{xy}}\right)^2 - \frac{1}{6}\left(\frac{r}{L_{xy}}\right)^3\right]\exp\left(-\frac{r}{L_{xy}} - \frac{|t|}{L_t}\right), \tag{A5}$$

in which r and t are the spatial distance and time difference between any two points of r_n, respectively, and the spatial dependency follows that proposed by Arhan and Colin de Verdière (1985). In the present study, we selected σ_h = 30 cm based on the OFES rms SSH value in the Kuroshio Extension region of our interest (see Fig. 1c), σ_ε = 3 cm based on the expected SWOT SSH noise level, and L_{xy} = 50 km and L_t = 3 days based on the spatial and temporal decorrelation scales of the OFES-simulated SSH field.

REFERENCES

Arhan, M., and A. Colin de Verdière, 1985: Dynamics of eddy motions in the eastern North Atlantic. *J. Phys. Oceanogr.*, **15**, 153–170, doi:10.1175/1520-0485(1985)015<0153:DOEMIT>2.0.CO;2.

Blumen, W., 1978: Uniform potential vorticity flow: Part I. Theory of wave interactions and two-dimensional turbulence. *J. Atmos. Sci.*, **35**, 774–783, doi:10.1175/1520-0469(1978)035<0774:UPVFPI>2.0.CO;2.

Buongiorno Nardelli, B., S. Guinehut, A. Pascual, Y. Drillet, S. Ruiz, and S. Mulet, 2012: Towards high resolution mapping of 3-D mesoscale dynamics from observations. *Ocean Sci.*, **8**, 885–901, doi:10.5194/os-8-885-2012.

Capet, X., J. C. McWilliams, M. J. Molemaker, and A. J. Shchepetkin, 2008: Mesoscale to submesoscale transition in the California Current system. Part I: Flow structure, eddy flux, and observational tests. *J. Phys. Oceanogr.*, **38**, 29–43, doi:10.1175/2007JPO3671.1.

Chelton, D. B., M. G. Schlax, and R. M. Samelson, 2011: Global observations of nonlinear mesoscale eddies. *Prog. Oceanogr.*, **91**, 167–216, doi:10.1016/j.pocean.2011.01.002.

Ducet, N., P.-Y. Le Traon, and G. Reverdin, 2000: Global high resolution mapping of ocean circulation from the combination of TOPEX/POSEIDON and *ERS-1/2*. *J. Geophys. Res.*, **105**, 19 477–19 498, doi:10.1029/2000JC900063.

Ferrari, R., and C. Wunsch, 2009: Ocean circulation kinetic energy: Reservoirs, sources, and sinks. *Annu. Rev. Fluid Mech.*, **41**, 253–282, doi:10.1146/annurev.fluid.40.111406.102139.

Fu, L.-L., and C. Ubelmann, 2014: On the transition from profile altimeter to swath altimeter for observing global ocean surface topography. *J. Atmos. Oceanic Technol.*, **31**, 560–568, doi:10.1175/JTECH-D-13-00109.1.

——, D. B. Chelton, P.-Y. Le Traon, and R. Morrow, 2010: Eddy dynamics from satellite altimetry. *Oceanography*, **23**, 14–25, doi:10.5670/oceanog.2010.02.

Gaultier, L., C. Ubelmann, and L.-L. Fu, 2016: The challenge of using future SWOT data for oceanic field reconstruction. *J. Atmos. Oceanic Technol.*, **33**, 119–126, doi:10.1175/JTECH-D-15-0160.1.

Gonzalez-Haro, C., and J. Isern-Fontanet, 2014: Global ocean current reconstruction from altimetric and microwave SST measurements. *J. Geophys. Res. Oceans*, **119**, 3378–3391, doi:10.1002/2013JC009728.

Guinehut, S., P. Y. Le Traon, G. Larnicol, and S. Philipps, 2004: Combining Argo and remote-sensing data to estimate the ocean three-dimensional temperature fields—A first approach based on simulated observations. *J. Mar. Syst.*, **46**, 85–98, doi:10.1016/j.jmarsys.2003.11.022.

Held, I. M., R. T. Pierrehumbert, S. T. Garner, and K. L. Swanson, 1995: Surface quasi-geostrophic dynamics. *J. Fluid Mech.*, **282**, 1–20, doi:10.1017/S0022112095000012.

Isern-Fontanet, J., J. B. Chapron, P. Klein, and G. Lapeyre, 2006: Potential use of microwave sea surface temperatures for the

estimation of ocean currents. *Geophys. Res. Lett.*, **33**, L24608, doi:10.1029/2006GL027801.

——, G. Lapeyre, P. Klein, B. Chapron, and M. Hecht, 2008: Three-dimensional reconstruction of oceanic mesoscale currents from surface information. *J. Geophys. Res.*, **113**, C09005, doi:10.1029/2007JC004692.

Klein, P., and G. Lapeyre, 2009: The oceanic vertical pump induced by mesoscale and submesoscale turbulence. *Annu. Rev. Mar. Sci.*, **1**, 351–375, doi:10.1146/annurev.marine.010908.163704.

——, B. L. Hua, G. Lapeyre, X. Capet, S. Le Gentil, and H. Sasaki, 2008: Upper ocean turbulence from high-resolution 3D simulations. *J. Phys. Oceanogr.*, **38**, 1748–1763, doi:10.1175/2007JPO3773.1.

——, J. Isern-Fontanet, G. Lapeyre, G. Roullet, E. Danioux, B. Chapron, S. Le Gentil, and H. Sasaki, 2009: Diagnosis of vertical velocities in the upper ocean from high resolution sea surface height. *Geophys. Res. Lett.*, **36**, L12603, doi:10.1029/2009GL038359.

LaCasce, J., and A. Mahadevan, 2006: Estimating subsurface horizontal and vertical velocities from sea-surface temperature. *J. Mar. Res.*, **64**, 695–721, doi:10.1357/002224006779367267.

Lapeyre, G., and P. Klein, 2006: Dynamics of the upper oceanic layers in terms of surface quasigeostrophy theory. *J. Phys. Oceanogr.*, **36**, 165–176, doi:10.1175/JPO2840.1.

——, ——, and B. L. Hua, 2006: Oceanic restratification forced by surface frontogenesis. *J. Phys. Oceanogr.*, **36**, 1577–1590, doi:10.1175/JPO2923.1.

Lévy, M., P. Klein, and A.-M. Treguier, 2001: Impacts of submesoscale physics on production and subduction of phytoplankton in an oligotrophic regime. *J. Mar. Res.*, **59**, 535–565, doi:10.1357/002224001762842181.

——, R. Ferrari, P. J. S. Franks, A. P. Martin, and P. Riviere, 2012: Bringing physics to life at the submesoscale. *Geophys. Res. Lett.*, **39**, L14602, doi:10.1029/2012GL052756.

Mahadevan, A., and D. Archer, 2000: Modeling the impact of fronts and mesoscale circulation on the nutrient supply and biogeochemistry of the upper ocean. *J. Geophys. Res.*, **105**, 1209–1225, doi:10.1029/1999JC900216.

Morrow, R., and P.-Y. Le Traon, 2012: Recent advances in observing mesoscale ocean dynamics with satellite altimetry. *Adv. Space Res.*, **50**, 1062–1076, doi:10.1016/j.asr.2011.09.033.

Mulet, S., M.-H. Rio, A. Mignot, S. Guinehut, and R. Morrow, 2012: A new estimate of the global 3D geostrophic ocean circulation based on satellite data and in-situ measurements. *Deep-Sea Res. II*, **77–80**, 70–81, doi:10.1016/j.dsr2.2012.04.012.

Noh, Y., and H. J. Kim, 1999: Simulations of temperature and turbulence structure of the oceanic boundary layer with the improved near-surface process. *J. Geophys. Res.*, **104**, 15 621–15 634, doi:10.1029/1999JC900068.

Onogi, K., and Coauthors, 2007: The JRA-25 Reanalysis. *J. Meteor. Soc. Japan*, **85**, 369–432, doi:10.2151/jmsj.85.369.

Pascual, A., S. Ruiz, B. Buongiorno Nardelli, S. Guinehut, D. Iudicone, and J. Tintoré, 2015: Net primary production in the Gulf Stream sustained by quasi-geostrophic vertical exchanges. *Geophys. Res. Lett.*, **42**, 441–449, doi:10.1002/2014GL062569.

Ponte, A. L., and P. Klein, 2013: Reconstruction of the upper ocean 3D dynamics from high-resolution sea surface height. *Ocean Dyn.*, **63**, 777–791, doi:10.1007/s10236-013-0611-7.

——, ——, X. Capet, P.-Y. Le Traon, B. Chapron, and P. Lherminier, 2013: Diagnosing surface mixed layer dynamics from high-resolution satellite observations: Numerical insights. *J. Phys. Oceanogr.*, **43**, 1345–1355, doi:10.1175/JPO-D-12-0136.1.

Qiu, B., and K. A. Kelly, 1993: Upper ocean heat balance in the Kuroshio Extension region. *J. Phys. Oceanogr.*, **23**, 2027–2041, doi:10.1175/1520-0485(1993)023<2027:UOHBIT>2.0.CO;2.

——, and S. Chen, 2005: Variability of the Kuroshio Extension jet, recirculation gyre, and mesoscale eddies on decadal timescales. *J. Phys. Oceanogr.*, **35**, 2090–2103, doi:10.1175/JPO2807.1.

——, ——, and P. Hacker, 2007: Effect of mesoscale eddies on subtropical mode water variability from the Kuroshio Extension System Study (KESS). *J. Phys. Oceanogr.*, **37**, 982–1000, doi:10.1175/JPO3097.1.

——, ——, P. Klein, H. Sasaki, and Y. Sasai, 2014: Seasonal mesoscale and submesoscale eddy variability along the North Pacific Subtropical Countercurrent. *J. Phys. Oceanogr.*, **44**, 3079–3098, doi:10.1175/JPO-D-14-0071.1.

Richman, J. G., B. K. Arbic, J. F. Shriver, E. J. Metzger, and A. J. Wallcraft, 2012: Inferring dynamics from the wavenumber spectra of an eddying global ocean model with embedded tides. *J. Geophys. Res.*, **117**, C12012, doi:10.1029/2012JC008364.

Rio, M.-H., S. Mulet, and N. Picot, 2014: Beyond GOCE for the ocean circulation estimate: Synergetic use of altimetry, gravimetry, and in situ data provides new insight into geostrophic and Ekman currents. *Geophys. Res. Lett.*, **41**, 8918–8925, doi:10.1002/2014GL061773.

Rudnick, D. L., 1996: Intensive surveys of the Azores Front: 2. Inferring the geostrophic and vertical velocity fields. *J. Geophys. Res.*, **101**, 16 291–16 303, doi:10.1029/96JC01144.

Sasaki, H., P. Klein, B. Qiu, and Y. Sasai, 2014: Impact of oceanic-scale interactions on the seasonal modulation of ocean dynamics by the atmosphere. *Nat. Commun.*, **5**, 5636, doi:10.1038/ncomms6636.

Smith, K. S., and J. Vanneste, 2013: A surface-aware projection basis for quasigeostrophic flow. *J. Phys. Oceanogr.*, **43**, 548–562, doi:10.1175/JPO-D-12-0107.1.

Stammer, D., 1997: Global characteristics of ocean variability estimated from regional TOPEX/POSEIDON altimeter measurements. *J. Phys. Oceanogr.*, **27**, 1743–1769, doi:10.1175/1520-0485(1997)027<1743:GCOOVE>2.0.CO;2.

Ubelmann, C., P. Klein, and L.-L. Fu, 2015: Dynamic interpolation of sea surface height and potential applications for future high-resolution altimetry mapping. *J. Atmos. Oceanic Technol.*, **32**, 177–184, doi:10.1175/JTECH-D-14-00152.1.

Wang, J., G. R. Flierl, J. H. LaCasce, J. L. McClean, and A. Mahadevan, 2013: Reconstructing the ocean's interior from surface data. *J. Phys. Oceanogr.*, **43**, 1611–1626, doi:10.1175/JPO-D-12-0204.1.

Wunsch, C., 1996: *The Ocean Circulation Inverse Problem*. Cambridge University Press, 442 pp.